Effects of constituent size on dislocation nucleation in macromolecular crystals

Ryo Suzuki[®], Kenichi Kojima, and Masaru Tachibana[®]

Graduate School of Nanobioscience, Yokohama City University, 22-2 Seto, Kanazawa-ku, Yokohama 236-0027, Japan



(Received 24 March 2025; revised 25 June 2025; accepted 23 July 2025; published 13 August 2025)

Understanding the deformation of materials at the nanoscale level provides insights into the incipient deformation process. Additionally, comprehending how a material deforms directly improves understanding of its mechanical properties. For atomic crystals such as metals and ceramics, direct observation of nanoscale deformation has clarified how materials deform and fracture while revealing the key factors governing the deformation process. However, in systems where the constituent elements themselves are significantly larger, understanding the deformation process is important not only for theoretical framework development but also for gaining new insights into deformation mechanisms. In this study, we investigated the deformation mechanisms of macromolecular crystals using protein crystals as a model, which consist of significantly larger molecular components than conventional atomic or small-molecule crystals. Through microscale indentation observation via x-ray topography, we revealed that plastic deformation occurs via the nucleation and motion of dislocations, which can be explained by the conventional dislocation theory. Nanoindentation experiments at a scale smaller than the molecular size of macromolecular crystals, along with estimations of the activation volume of dislocations, demonstrated that the molecules deform slightly at the incipient stage before dislocation nucleation. This finding indicates that the size of the constituents in materials affects material deformation, and it suggests the potential for expanding deformation mechanisms by considering the characteristics of the constituent components.

DOI: 10.1103/9pjv-958d

I. INTRODUCTION

Understanding the elastic-plastic transition and deformation mechanisms that govern the mechanical properties of materials is crucial for establishing guidelines for the application and design of new materials. To date, studies on material strength through macroscopic tensile and compression tests as well as investigations of incipient deformation behavior via indentation methods have been conducted for metals, ceramics, and semiconductor materials [1].

Nanoindentation is one of the most effective techniques for observing material deformation at the atomic or nanoscale. In nanoindentation, the deformation of materials under an applied load is detected using a load-displacement (P-h) curve [2]. Recent advancements in nanoindentation equipment have enabled examination of the dislocation behavior of brittle materials [3–5]. Materials initially undergo elastic deformation under a certain load and then plastic deformation, leaving a permanent strain. By closely examining the transition from elastic to plastic deformation, the nucleation and motion of dislocations can be quantified. In addition to experimental approaches, molecular dynamics simulations have been increasingly used to elucidate material deformation mechanisms [6–13]. Understanding how materials deform and investigating the factors that govern deformation as well as the underlying mechanisms provide fundamental insights into material behavior and aid the development of new materials.

Crystals are solids in which atoms or small molecules are arranged in a highly ordered structure. In crystalline mate-

*Contact author: rsuzuki@yokohama-cu.ac.jp

rials, plastic deformation due to dislocations plays a crucial role in material deformation, as mentioned above. This deformation mechanism is characterized by the bonding and crystal structure of the material. In contrast to inorganic crystals with atomic-scale periodic structures, protein crystals are single crystals composed of biomacromolecules with sizes of dozens of nanometers [14]. Their lattice constants exceed 10 nm, making their unit cells significantly larger than those of atomic and low-molecular-weight crystals. In the dislocation theory, the self-energy of dislocation E is expressed as $E \sim \mu |\mathbf{b}|^2$ [15]. In protein crystals, which have a relatively low shear modulus μ and an enormous Burgers vector \mathbf{b} , dislocations can energetically stably nucleate and multiply to govern plastic deformation, which presents an interesting mechanical concept.

Thus far, dislocations introduced during crystallization have been observed in several types of protein crystals, such as hen egg-white lysozyme and glucose isomerase [16–18]. Observations of slip traces via Vickers microindentation suggest that the deformation of macromolecular crystals is controlled by the dislocation mechanism [19–22]. Additionally, dislocations can be introduced via simple stress loading using a sewing needle [23]. However, knowledge regarding the nucleation of dislocations such as half-loop dislocations remains limited.

In this study, we applied the nanoindentation technique to macromolecular crystals with weak interactions such as van der Waals forces, water-mediated hydrogen bonding, and electrostatic interactions. Glucose isomerase (GI) crystals were used as a model of macromolecular crystals because they can be grown with no grown-in dislocations and high crystallinity. We investigated the plastic deformation mechanisms

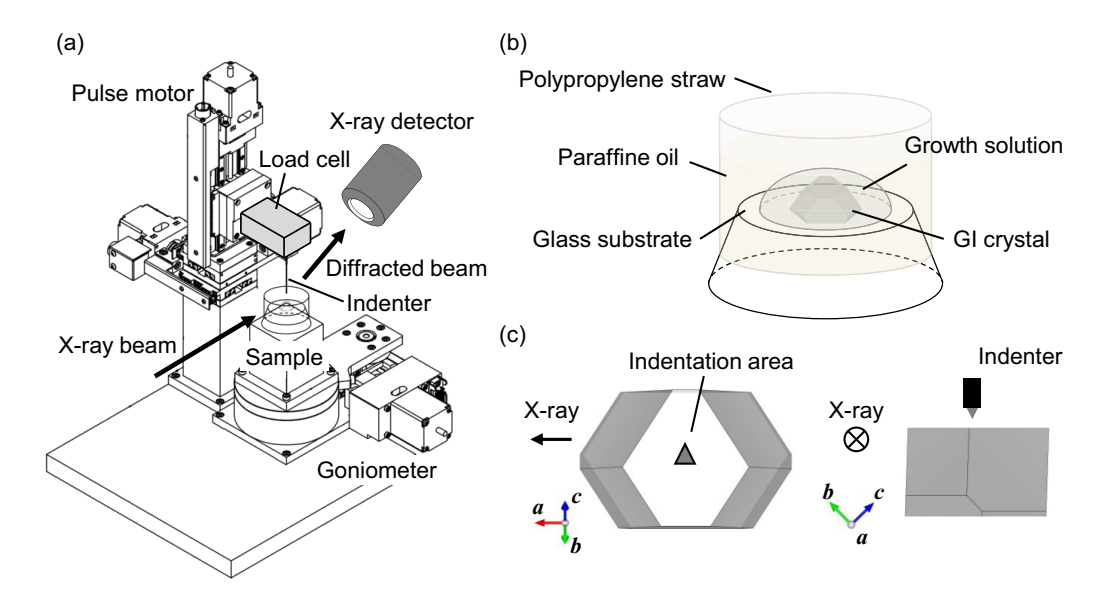


FIG. 1. (a) Experimental setup of the indentation in the beamline at PF. The Berkovich indenter with a load cell was set within a handmade apparatus using a pulse motor. (b) Schematic of the GI crystal in the growth solution on a glass substrate sealed with paraffin oil in a polypropylene straw. (c) Geometry of the indentation. The indenter is on the (011) surface of the GI crystal and the x-ray enters in the direction along the *a* axis. The schematics of the crystal morphology were prepared using the VESTA software [27].

of macromolecular crystals during indentation through *in situ* synchrotron x-ray topography. Furthermore, we examined the incipient deformation mechanisms of crystalline materials composed of macromolecules such as protein crystals by using nanoindentation techniques.

II. METHODS

A. Materials

GI crystals were grown using GI solutions containing industrial-grade GipF (Nagase Sanbio Co., Ltd.). Purification was conducted via dialysis using a membrane (MWCO: 500– 1000 Da) in distilled water for 1 d. The GI solution was then concentrated using polyethylene glycol (PEG 20 000) for half a day to reduce the distilled water. Subsequently, the GI solution was filtered using a 0.1 µm sized membrane filter (PALL ACRO DISC, Japan). The concentration of GI in the solution was determined by measuring the absorption of 280 nm wavelength light using a UV-visible spectrophotometer (NanoDrop One, Thermo Fisher Scientific, Inc.). Large GI crystals of 2-3 mm in size were grown using a seeding method as follows: seed crystals were grown via a hanging drop technique at 294 K using a crystallization solution containing 50 mg/mL GI, 0.6 M ammonium sulfate, 1 mM magnesium sulfate, and 6 mM tris(hydroxymethyl)aminomethane hydrochloride (pH 7.0), as referred [24,25]. Each seed crystal was subsequently placed in a crystallization droplet on siliconized glass (ϕ 12 mm, 220 µm thickness) attached to an acrylic holder, as performed previously [24,25]. The droplets on the holder were annealed at 313 K for 10 min to prevent heterogeneous nucleation. After annealing, the samples were maintained at 294 K for two weeks. The resultant GI crystals had a body-centered orthorhombic structure with space group 1222, where lattice constants a, b, and c were 9.39, 9.97, and 10.29 nm, respectively [26].

B. In situ observation of indentation by x-ray topography

For the *in situ* observation of indentation, a handmade indentation system was installed in the BL14B and BL20B beamlines at the Photon Factory (PF) of the High Energy Accelerator Research Organization, as shown in Fig. 1(a). Indentation tests were conducted using an indentation system by assembling pulse motor stages (YA05A-R1 and XA05A-L2-2H, Kohzu) and a load cell (ZTS-DPU-5N, IMADA). A Berkovich diamond indenter was attached to the load cell. The motion of the indenter with the load cell was controlled by pulse motor stages and a stage controller (SC-410, Kohzu). The Hertzian elastic fitting method [28,29] was adopted to calibrate the radius of the used diamond indenter.

X-ray topography was performed using synchrotron radiation at the BL14B and BL20B beamlines. A monochromatic beam of 1.2 Å was selected by adjusting the doublecrystal monochromator. The size of the incident beam (horizontal × vertical) was 5 mm × 14 mm, which was sufficient to cover the entire crystal. During the indentation tests, the GI crystals in the crystallization solution on the glass substrate were sealed with paraffin oil in a polypropylene straw, as shown in Fig. 1(b). The sealed GI crystals were mounted onto a precision goniometer. The loading and unloading rates were both set to 200 nm/s. The GI crystal was loaded to the maximum load over a period of 85 seconds, and then unloaded to zero over the following 85 seconds. In this study, indentation was performed on the (011) surface of the GI crystals, as shown in Fig. 1(c). During indentation, the diffraction images were recorded using a high-spatial-resolution, 2D, digital CCD camera (Photonic Science X-RAY FDI 1.00:1, effective pixel size: $6.45 \times 6.45 \,\mu\text{m}^2$). To analyze the diffraction images precisely after indentation, the diffractions were recorded using x-ray films (Agfa D2). The spatial resolution of x-ray films is a few micrometers, which is higher than that of x-ray CCD cameras. The samples were not polished owing to the brittleness and fragility of the protein crystals.

C. Nanoindentation tests

All indentation tests were performed using a nanoindentation system (TI Premier, Bruker) with a Berkovich diamond tip (tip radius of 72 nm) at 296 K. Before the indentation tests, the system was calibrated using fused silica. The tip of the Berkovich indenter was assumed to have a finite radius due to manufacturing imperfections and tip rounding. Thus, the Hertzian model, which is based on a spherical tip approximation, was considered appropriate for analyzing the initial elastic response, and the tip radius was identified by comparing the ideal elastic Hertzian load-displacement curve (P-h curve) with experimental data [28,29]. This approach has been widely adopted in previous nanoindentation studies under similar conditions [4,5,10,11]. To prevent drying, the GI crystals were maintained in the crystallization solution during the indentation tests. The sample was loaded to the maximum extent for 5 s, followed by 2 s of load holding and 5 s of unloading to zero. The average loading rate was 25 μ N/s.

D. Determination of elastic constants by ultrasound velocity measurements

The sound velocities of the GI crystals were measured using the ultrasonic pulse-echo method with an ultrasonic pulse/receiver (PR35, JSR Ultrasonics). Transverse and longitudinal ultrasonic transducers with frequencies of 5 and 18 MHz, respectively, were used. A shear gel was used as an adhesive to glue the GI crystals to the transducers to ensure close contact between them. To improve the brittleness of the GI crystals during contact, chemical crosslinking using glutaraldehyde was performed, as referred [17]. As mentioned in the Materials section, the GI crystals have a body-centered orthorhombic structure with a space group of I222, where lattice constants a, b, and c are 9.39, 9.97, and 10.29 nm, respectively [26]. The ratio of the lattice constants is 1.00:1.06:1.09, and the GI crystals can be regarded as a body-centered cubic (BCC) structure. The propagation/polarization directions of the longitudinal sound velocity v_1 and transverse sound velocities v_2 and v_3 were [110]/[110], [110]/[001], and [110]/[1 $\bar{1}$ 0], respectively. Thus, the relationship between sound velocity and elastic constants is as follows [30]:

$$\rho v_1^2 = \frac{1}{2}(C_{11} + C_{12} + 2C_{44}), \quad \rho v_2^2 = C_{44},$$

$$\rho v_3^2 = \frac{1}{2}(C_{11} - C_{12}), \tag{1}$$

where ρ is the density of GI crystals, calculated as 1.15 Mg/m³. Density ρ was calculated as follows:

$$\rho = \frac{m_{\rm m} + m_{\rm w}}{V_{\rm u}},\tag{2}$$

where $m_{\rm m}$ and $m_{\rm w}$ are the masses of the GI and water molecules in a unit cell, respectively, and $V_{\rm u}$ is the unit-cell volume of the GI crystal. Mass $m_{\rm w}$ was estimated via Matthews' method [31] using structural analysis data (PDB ID: 1XIB) [26]. Thus, elastic constants C_{11} , C_{12} , and C_{44} were simply determined from the BCC structure.

E. Quantum calculation of molecular volume of amino acids

The molecular volume of the amino acids was calculated using density functional theory (DFT). Geometric

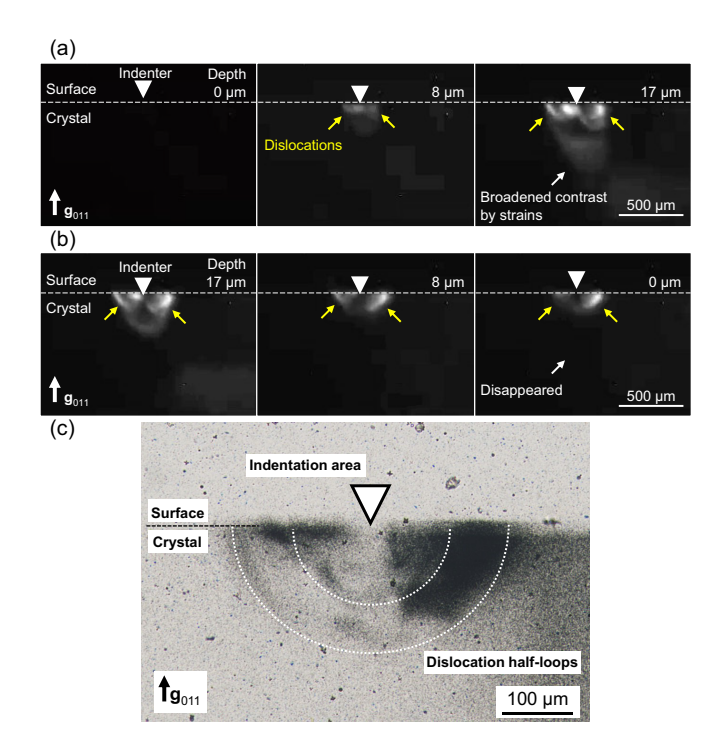


FIG. 2. Series of x-ray topographs during the (a) loading and (b) unloading processes of the indentation. (c) X-ray topograph captured using an x-ray film after the indentation. The half-loop contrasts due to the induced dislocations are clearly observed. The white triangle corresponds to the indenter position.

optimization of the calculated amino acids such as alanine, leucine, aspartic acid, glycine, and arginine was performed at the DFT level and the B3LYP/6–31G(d) level using the Gaussian 16 package. The volume of the amino acid molecules was estimated using the optimized structure. Amino acids were selected based on the amino acid sequence of GI molecules using structural analysis data [26]. The selected amino acids are abundant in GI molecules.

III. RESULTS

A. In situ observations of stress-induced dislocations

Figure 2(a) shows a series of x-ray topographs captured during loading using the indentation apparatus. A white contrast appeared beneath the indentation tip when it was in contact with the crystal surface. Subsequently, half-loop contrasts appeared around the indentation area. During indentation, the size of the half-loop contrast increased. At the maximum indentation depth of 17 μ m and the maximum load of 15 mN, some half-loop contrasts appeared with depths of 170 μ m, ten times larger than the indentation depth. Moreover, white broadened contrasts appeared at a depth of 500 μ m.

Figure 2(b) shows a series of topographs captured during the unloading process. The broadened contrasts with depths of 500 µm disappeared with unloading. This implies that the broadened contrasts were associated with the elastic strain caused by the load. In contrast, the half-loop contrasts with depths of 170 µm were clearly observed after unloading. These contrasts correspond to the induced dislocations

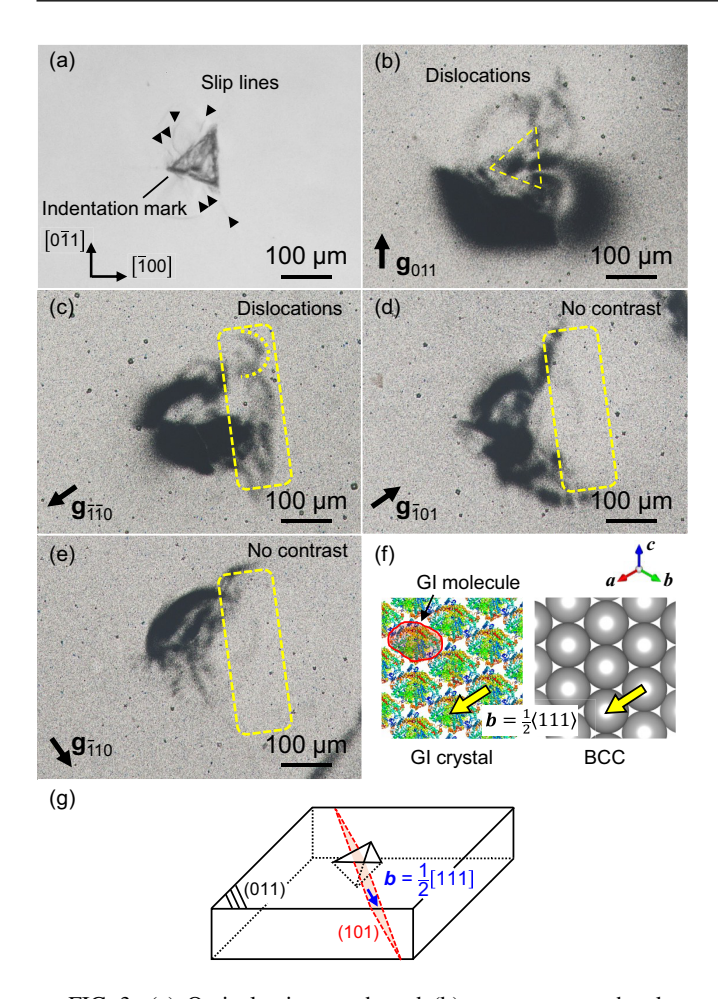


FIG. 3. (a) Optical micrograph and (b) x-ray topograph taken using x-ray film with g=011 after the indentation. X-ray topographs taken using x-ray film with (c) $g=\bar{1}\bar{1}0$, (d) $g=\bar{1}01$, and (e) $g=\bar{1}10$. (f) Schematic of the molecular arrangement of the GI crystal (left) and a BCC crystal such as Fe (right) viewed along the [111] direction. The yellow arrows in (f) correspond to the typical Burgers vector $1/2\langle 111 \rangle$ in the BCC structure. (g) Schematic of the identified slip system.

associated with plastic deformation. Figure 2(c) shows the x-ray topographs of the x-ray film after indentation. Half-loop contrasts were clearly observed in relation to those in the image captured by the x-ray CCD camera. Thus, *in situ* x-ray topography confirmed that dislocations were introduced by stress application.

B. Analysis of dislocations

Figures 3(a)-3(d) depict an optical micrograph and x-ray topograph after the indentation test. As shown in Fig. 3(a), a triangular mark corresponding to the Berkovich tip and some line shape contrasts around the indentation mark are observed (indicated by black triangles). The line contrasts appear to correspond to the slip lines associated with slip deformation caused by dislocation motion. Moreover, dislocation contrast around the indentation mark was observed in the x-ray topograph, as shown in Fig. 3(b). The contrasts extended to an area larger than the size of the indentation mark shown in Fig. 3(a).

This is due to the strain around the dislocations associated with plastic deformation.

Figures 3(c)-3(e) show the x-ray topographs captured with various diffraction vectors, specifically $\mathbf{g} = \bar{1}\bar{1}0$, $\bar{1}01$, and $\bar{1}10$. As shown in Fig. 3(c), half-loop contrasts associated with dislocations are clearly observed. Conversely, the half-loop contrasts disappear at $\mathbf{g} = \bar{1}01$ and $\bar{1}10$. The invisibility of the contrasts depending on the diffraction vector indicates that the contrasts correspond to dislocations. According to the invisibility criterion for dislocation images [32], the Burgers vector of the dislocations is [111]. The shortest translational vector of [111] in a body-centered orthorhombic crystal corresponds to half of the body diagonal. Therefore, the Burgers vector was assigned a value of 1/2[111] (|b| = 8.56 nm). The other contrasts could not be assigned because they did not disappear owing to the large deformations. The GI crystals had a body-centered orthorhombic structure with space group *I*222, where lattice constants a, b, and c were 9.39, 9.97, and 10.29 nm, respectively [26]. The ratio of the lattice constants was 1.00:1.06:1.09, and the GI crystals can be regarded as BCC structures. To compare the BCC crystals, the schematics of the molecular arrangement and slip system are shown in Figs. 3(f) and 3(g), respectively. In BCC materials, the translational vector 1/2 (111) is dominated by the Burgers vector [15]. Thus, a Burgers vector of 1/2[111] was reasonable for the GI crystals.

C. Verification of plastic deformation behavior by nanoindentation

The incipient plasticity of GI crystals was investigated using the nanoindentation method. Figures 4(a) and 4(b) show a typical load-displacement curve (P-h curve) obtained for the (011) surface via nanoindentation tests. Figure 4(b) depicts an enlarged view of the vicinity of the origin of Fig. 4(a). To analyze the behavior of the elastic and plastic deformation, the P-h curve was fitted using the Hertzian curve. Based on the Hertzian solution [28,29], the purely elastic relationship between the load and displacement can be described as follows:

$$P = \frac{4}{3} E_r \sqrt{R} h^{3/2}, \tag{3}$$

where P is the load, E_r is the reduced modulus, R is the tip radius (72 nm), and h is the displacement. The reduced modulus, E_r , was theoretically calculated from the elastic modulus and Poisson's ratio of the indenter and sample as follows:

$$\frac{1}{E_r} = \frac{1 - \nu_i^2}{E_i} + \frac{1 - \nu_s^2}{E_s},\tag{4}$$

where $E_i = 1140 \,\text{GPa}$, $v_i = 0.07$ for the diamond of the Berkovich tip, $E_s = 1.25 \,\text{GPa}$, and $v_s = 0.44$ for the GI crystal. It is noted that the Young's modulus E_s and the Poisson's ratio v_s of the GI crystals are calculated using elastic constants $C_{11} = 4.37 \,\text{GPa}$, $C_{12} = 3.46 \,\text{GPa}$, and $C_{44} = 0.42 \,\text{GPa}$, which are experimentally determined from the ultrasound velocity measurements (see Table I and Fig. 5). Consequently, we obtained $E_r = 1.55 \,\text{GPa}$ as the calculated value.

The blue line indicates the Hertzian elastic fit, and the initial P-h curve was well fitted, as shown in Fig. 4(b). A deviation from the elastic fit is clearly observed in the P-h

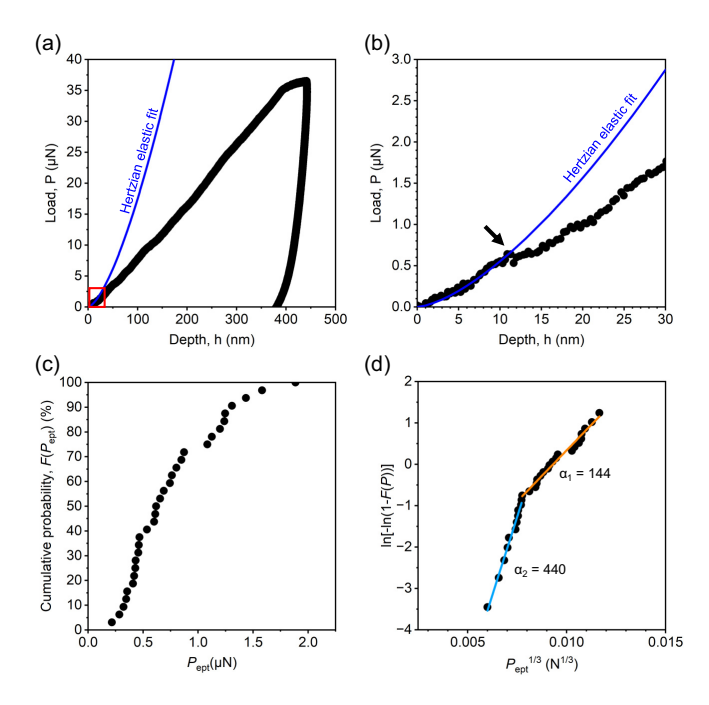


FIG. 4. (a) Typical P-h curve of GI crystals. (b) Enlarged figure of the vicinity of the origin of (a). The red line indicates the Hertzian elastic fitting. The elastic-to-plastic deformation appears clearly (indicated as a black arrow), deviating from the elastic fit. (c) Cumulative probability of the elastic-plastic transition load, $P_{\rm ept}$. (d) Relationship between $P_{\rm ept}^{1/3}$ and $\ln[-\ln(1-F(P))]$.

curve, as indicated by the black arrow. The displacement at the deviated point is considered to be an elastic-to-plastic transition, although we cannot see a clear pop-in event. The elastic-to-plastic transition load is referred to as $P_{\rm ept}$ in this study. Generally, critical shear stress corresponds to the shear strength of a material [12]. The load at the elastic-plastic transition, $P_{\rm ept}$, can be converted into the maximum shear stress, $\tau_{\rm max}$, beneath the indenter during deformation as follows [33,34]:

$$\tau_{\text{max}} = 0.31 \left(\frac{6E_r^2}{\pi^3 R^2} P_{\text{ept}} \right)^{1/3}.$$
(5)

Figure 4(c) shows the cumulative probability $[F(P_{\rm ept})]$ of $P_{\rm ept}$. To clarify the dislocation nucleation, 50 indents were performed, and the maximum shear stresses were obtained from at least 30 valid data points. The values of $P_{\rm ept}$ varied from 0.22 to 1.89 μN , as seen in Fig. 4(c). Consequently,

TABLE I. Mechanical properties of the GI crystals determined from ultrasound velocity measurements.

Elastic constants (GPa)	C_{11}	4.37
	C_{12}	3.46
	C_{44}	0.42
Young's modulus (GPa)	arepsilon	1.25
Shear modulus (GPa)	μ	0.43
Bulk modulus (GPa)	κ	3.76
Compressibility ($\times 10^{-9}/Pa$)	$oldsymbol{eta}$	0.27
Poisson's ratio	$\sigma_{ m s}$	0.44

the values of all maximum shear stresses varied from 83 to 171 MPa. The average and standard deviation of $\tau_{\rm max}$ were 127 \pm 22 MPa. To compare the shear strengths, the shear modulus G of the GI crystal was calculated to be 430 MPa as follows:

$$G = \frac{E_s}{2(1 + \nu_s)},\tag{6}$$

where $E_s = 1.25$ GPa and $v_s = 0.44$, as mentioned above. In common materials such as metals and semiconductors, the critical shear stress is close to the ideal shear strength of $G/2\pi$ [15]. For GI crystals, the ideal shear strength is calculated as 69 MPa, and the order of $\tau_{\rm max}$ shows good agreement with the ideal shear strength $G/2\pi$, whereas $\tau_{\rm max}$ is slightly higher. This discrepancy may be related to the unique activation volume of the GI crystals, as discussed below.

The activation volume of the dislocation is defined as the derivative of the activation free energy with stress. It is a volumetric parameter affected by the applied stress when the dislocation motion in plastic deformation is described as the mechanical work of indentation and/or thermal activation processes. This is related to the energy change due to the applied stress and plays an important role in determining the energy required to overcome the potential due to the lattice defects that govern the motion of dislocations. Specifically, the nucleation rate of dislocation \dot{n} is statistically described as follows [35]:

$$\dot{n} = \dot{n}_0 \exp\left(-\frac{\varepsilon - \sigma V}{k_{\rm B}T}\right),\tag{7}$$

where \dot{n}_0 is the attempt frequency per unit volume, ε is the activation energy, σ is the stress, V is the activation volume, and the thermal energy is Boltzmann's constant $k_{\rm B}$ multiplied by temperature T. By adopting the method developed by Schuh et~al.~[35,36],~V for dislocations can be evaluated as unknown adjustable parameters. Cumulative probability $F(P_{\rm ept})$ is converted using $\ln[-\ln(1-F(P_{\rm ept}))]$ vs $P_{\rm ept}^{1/3}$, as shown in Fig. 4(d). According to this method, the fitting function is as follows:

$$\ln\left[\ln\left(\frac{1}{1 - F(P_{\text{ept}})}\right)\right] = \alpha P_{\text{ept}}^{1/3} + \beta \tag{8}$$

and

$$\alpha = \frac{0.47}{\pi} \left(\frac{4E_r}{3R}\right)^{2/3} \frac{V}{k_{\rm B}T},\tag{9}$$

where $F(P_{\rm ept})$ is the cumulative probability, $P_{\rm ept}$ is the load of elastic-to-plastic transition, E_r is the reduced modulus (1.55 GPa), R is the tip radius (72 nm), V is the activation volume of the dislocation, $k_{\rm B}$ is the Boltzmann constant (1.38 × 10⁻²³ J/K), and T is the temperature (296 K in this study). In Eq (8), parameter β is of weak P dependence in relation to the first term, $\alpha P_{\rm ept}^{1/3}$, as reported [36]. Thus, we can estimate the activation volume of dislocation using the value of slope α . As shown in Fig. 4(d), $F(P_{\rm ept})$ can be divided into two parts with different slopes. By fitting the two parts, the slopes were obtained as 495 and 1508; therefore, the activation volumes of the dislocations were estimated as 144 and 439 ų, respectively.

Based on this model, the activation volume of dislocations was extracted from the experimental data. The estimated

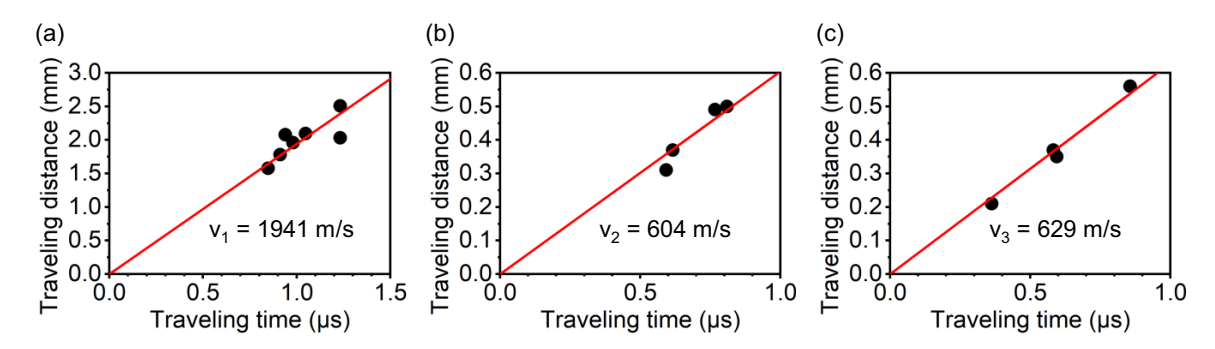


FIG. 5. Relationship between traveling distance and traveling time for three sound velocities. The wave type and propagation/polarization direction are (a) longitudinal, [110]/[110], (b) transverse, [110]/[001], and (c) transverse, [110]/[110], respectively. The linear fitting corresponds to the extrapolated line of distance vs time.

values of the activation volume are 144 and 439 Å³; however, they are much smaller than the cubed Burgers vector $|\mathbf{b}|^3$ (calculated as $6.27 \times 10^5 \,\text{Å}^3$). It seems unlikely that the present data correspond to the homogeneous nucleation of a dislocation loop beneath the indenter because the estimated activation volume has a large discrepancy in size with respect to the dislocation loop, such as the cubed Burgers vector and the observed dislocations, as shown in Fig. 3. Moreover, the activation volume is considerably smaller than that of a GI molecule, estimated as $2.68 \times 10^5 \,\text{Å}^3$. This suggests that the estimated activation volume may correspond to the deformation of some protein molecules, i.e., amino acid residues, beneath the indenter. The volumes of amino acid molecules such as alanine and leucine, which are abundantly present in GI molecules, are 109 and 184 Å³, respectively, as estimated by quantum calculations. These values are listed in Table II, and they are similar to those of the activation volumes of the dislocations, 144 and 439 Å³. Previous studies on atomic crystals such as metals using the nanoindentation method have estimated the activation volume [35,36]. This was smaller than the size of the expected dislocation loop. It has been shown that dislocations can nucleate at a preexisting vacancy and/or vacancy cluster because the estimated activation volume is on the order of 0.5b³ [35]. In contrast, for GI crystals, the vacancy size is expected to reach the GI molecular size of $2.68 \times 10^5 \,\text{Å}^3 \,(\sim 0.4 \,\text{b}^3)$ as mentioned earlier. This value is significantly larger than the estimated activation volume ($\sim 0.7 \times 10^{-3} \, b^3$). Therefore, we suggest that the initial stage of plastic deformation in macromolecular

TABLE II. Calculated volume of amino acid molecules contained in GI molecules. Note that the content refers to the ratio of amino acids to all amino acids composed of the GI molecules.

Amino acid	Content (%)	Volume (Å ³)
Alanine	12.1	109
Leucine	10.1	184
Aspartic acid	9.5	118
Glycine	9.5	98
Arginine	9.0	194

crystals is controlled by the deformation of the molecules themselves, followed by lattice deformation associated with the dislocation mechanism. A size-scale effect can be defined as a change in material properties, particularly material strength and plasticity, and the sample dimensions are a key factor [37,38]. This study clarified that the constituent size effect is induced during the incipient deformation process in macromolecular crystals.

IV. CONCLUSIONS

We successfully clarified the deformation behavior of macromolecular crystals. Based on the indentation test results and *in situ* x-ray topography observations, we demonstrated that plastic deformation is mainly controlled by dislocation nucleation and multiplication in protein crystals. It is remarkable that the elastic-to-plastic transition appears on the order of micronewtons. The findings presented herein suggest that deformation may begin with the molecules themselves during the incipient deformation of macromolecular crystals. Further, there is potential for expanding deformation mechanisms by considering the characteristics of the constituent components.

ACKNOWLEDGMENTS

This work was financially supported by JST PRESTO (JPMJPR1995) and JSPS KAKENHI (19K23579, 21K04654, 23H01305, 23K26000, and 25K08281). The x-ray topography measurements were performed at BL14B and BL20B of the Photon Factory of KEK with the approval of the Program Advisory Committee (Proposals 2021G022, 2023G030, and 2025G074).

DATA AVAILABILITY

The data that support the findings of this article are openly available [39].

- [1] M. A. Meyers and K. K. Chawla, *Mechanical Behavior of Materials*, 2nd ed. (Cambridge University Press, Cambridge, 2008).
- [2] W. C. Oliver and G. M. Pharr, An improved technique for determining hardness and elastic modulus using load and displacement sensing indentation experiments, J. Mater. Res. 7, 1564 (1992).
- [3] M. A. Lodes, A. Hartmaier, M. Göken, and K. Durst, Influence of dislocation density on the pop-in behavior and indentation size effect in CaF₂ single crystals: Experiments and molecular dynamics simulations, Acta Mater. **59**, 4264 (2011).
- [4] X. Fang, K. Ding, S. Janocha, C. Minnert, W. Rheinheimer, T. Frömling, K. Durst, A. Nakamura, and J. Rödel, Nanoscale to microscale reversal in room-temperature plasticity in SrTiO₃ by tuning defect concentration, Scr. Mater. 188, 228 (2020).
- [5] A. Nakamura, X. Fang, A. Matsubara, E. Tochigi, Y. Oshima, T. Saito, T. Yokoi, Y. Ikuhara, and K. Matsunaga, Photoindentation: A new route to understanding dislocation behavior in light, Nano Lett. 21, 1962 (2021).
- [6] C. L. Kelchner, S. J. Plimpton, and J. C. Hamilton, Dislocation nucleation and defect structure during surface indentation, Phys. Rev. B 58, 11085 (1998).
- [7] J. Li, K. J. Van-Vliet, T. Zhu, S. Yip, and S. Suresh, Atomistic mechanisms governing elastic limit and incipient plasticity in crystals, Nature (London) 418, 307 (2002).
- [8] O. Rodríguez de la Fuente, J. A. Zimmerman, M. A. González, J. de la Figuera, J. C. Hamilton, W. W. Pai, and J. M. Rojo, Dislocation emission around nanoindentations on a (001) fcc metal surface studied by scanning tunneling microscopy and atomistic simulations, Phys. Rev. Lett. 88, 036101 (2002).
- [9] J. Knap and M. Ortiz, Effect of indenter-radius size on Au(001) nanoindentation, Phys. Rev. Lett. 90, 226102 (2003).
- [10] V. Navarro, O. Rodríguez de la Fuente, A. Mascaraque, and J. M. Rojo, Uncommon dislocation processes at the incipient plasticity of stepped gold surfaces, Phys. Rev. Lett. 100, 105504 (2008)
- [11] R. J. Wagner, L. Ma, F. Tavazza, and L. E. Levine, Dislocation nucleation during nanoindentation of aluminum, J. Appl. Phys. 104, 114311 (2008).
- [12] C. Begau, A. Hartmaier, E. P. George, and G. M. Pharr, Atomistic processes of dislocation generation and plastic deformation during nanoindentation, Acta Mater. 59, 934 (2011).
- [13] S. Lee, A. Vaid, J. Im, B. Kim, A. Prakash, J. Guénolé, D. Kiener, E. Bitzek, and S. H. Oh, In-situ observation of the initiation of plasticity by nucleation of prismatic dislocation loops, Nat. Commun. 11, 2367 (2020).
- [14] N. E. Chayen, J. R. Helliwell, and E. H. Snell, *Macromolecular Crystallization and Crystal Perfection* (Oxford University Press, Oxford, 2010).
- [15] J. P. Hirth and J. Lothe, *Theory of Dislocations*, 2nd ed. (Wiley, New York, 1982).
- [16] Y. Mukobayashi, N. Kitajima, Y. Yamamoto, K. Kajiwara, H. Sugiyama, K. Hirano, K. Kojima, and M. Tachibana, Observation of dislocations in hen-egg white lysozyme crystals by synchrotron monochromatic-beam X-ray topography, Phys. Status Solidi A 206, 1825 (2009).
- [17] R. Suzuki, H. Koizumi, K. Kojima, S. Fukuyama, Y. Arai, K. Tsukamoto, Y. Suzuki, and M. Tachibana, Characterization of grown-in dislocations in high-quality glucose isomerase

- crystals by synchrotron monochromatic-beam X-ray topography, J. Cryst. Growth **468**, 299 (2017).
- [18] R. Suzuki, M. Abe, K. Kojima, and M. Tachibana, Identification of grown-in dislocations in protein crystals by digital X-ray topography, J. Appl. Cryst. **54**, 163 (2021).
- [19] H. Koizumi, H. Kawamoto, M. Tachibana, and K. Kojim, Effect of intracrystalline water on micro-Vickers hardness in tetragonal hen egg-white lysozyme single crystals, J. Phys. D Appl. Phys. 41, 074019 (2008).
- [20] R. Suzuki, T. Kishi, S. Tsukashima, M. Tachibana, K. Wako, and K. Kojima, Hardness and slip systems of orthorhombic hen egg-white lysozyme crystals, Phil. Mag. 96, 2930 (2016).
- [21] T. Kishi, R. Suzuki, C. Shigemoto, H. Murata, K. Kojima, and M. Tachibana, Microindentation hardness of protein crystals under controlled relative humidity, cryst. 7, 339 (2017).
- [22] R. Suzuki, C. Shigemoto, M. Abe, K. Kojima, and M. Tachibana, Analysis of slip systems in protein crystals with a triclinic form using a phenomenological macro-bond method, CrystEngComm 23, 3753 (2021).
- [23] R. Suzuki, M. Tachibana, H. Koizumi, and K. Kojima, Direct observation of stress-induced dislocations in protein crystals by synchrotron X-ray topography, Acta Mater. 156, 479 (2018).
- [24] R. Suzuki, H. Koizumi, K. Hirano, T. Kumasaka, and M. Tachibana, Analysis of oscillatory rocking curve by dynamical diffraction in protein crystals, Proc. Natl. Acad. Sci. USA. 115, 3634 (2018).
- [25] R. Suzuki, M. Abe, K. Hirano, K. Kojima, and M. Tachibana, Rocking-curve imaging of high-quality protein crystals by nondispersive X-ray optics in the double-crystal configuration, J. Appl. Cryst. 55, 1111 (2022).
- [26] H. L. Carrell, H. Hoier, and J. P. Glusker, Modes of binding substrates and their analogues to the enzyme D-xylose isomerase, Acta Cryst. D **50**, 113 (1994).
- [27] K. Momma and F. Izumi, VESTA 3 for three-dimensional visualization of crystal, volumetric and morphology data, J. Appl. Cryst. 44, 1272 (2011).
- [28] W. Li, H. Bei, J. Qu, and Y. Gao, Effects of machine stiffness on the loading-displacement curve during spherical nanoindentation, J. Mater. Res. 28, 1903 (2013).
- [29] W. C. Oliver and G. M. Pharr, Measurement of hardness and elastic modulus by instrumented indentation: Advances in understanding and refinements to methodology, J. Mater. Res. 19, 3 (2004).
- [30] C. Kittel, *Introduction to Solid State Physics*, 8th ed. (Wiley, New York, 2004).
- [31] B. W. Matthews, Solvent content of protein crystals, J. Mol. Biol. 33, 491 (1968).
- [32] D. K. Bowen and B. K. Tanner, *High-Resolution X-ray Diffractometry and Topography* (Taylor & Frances, London, 1998).
- [33] K. L. Johnson, Contact Mechanics (Cambridge University Press, Cambridge, 1985).
- [34] J. R. Morris, H. Bei, G. M. Pharr, and E. P. George, Size effects and stochastic behavior of nanoindentation pop in, Phys. Rev. Lett. **106**, 165502 (2011).
- [35] C. A. Schuh, J. K. Mason, and A. C. Lund, Quantitative insight into dislocation nucleation from high-temperature nanoindentation experiments, Nat. Mater. 4, 617 (2005).

- [36] J. K. Mason, A. C. Lund, and C. A. Schuh, Determining the activation energy and volume for the onset of plasticity during nanoindentation, Phys. Rev. B 73, 054102 (2006).
- [37] M. D. Uchic, D. M. Dimiduk, J. N. Florando, and W. D. Nix, Sample dimensions influence strength and crystal plasticity, Science **305**, 986 (2004).
- [38] R. Maaß, S. V. Petegem, D. Ma, J. Zimmermann, D. Grolimund, F. Roters, H. V. Swygenhoven, and D. Raabe, Smaller is stronger: The effect of strain hardening, Acta Mater. 57, 5996 (2009).
- [39] Dataset available at https://doi.org/10.5281/zenodo. 16406174.